

Detection of a particle shower at the Glashow resonance with IceCube

<https://doi.org/10.1038/s41586-021-03256-1>

The IceCube Collaboration*

Received: 28 July 2020

Accepted: 18 January 2021

Published online: 10 March 2021

 Check for updates

The Glashow resonance describes the resonant formation of a W^- boson during the interaction of a high-energy electron antineutrino with an electron¹, peaking at an antineutrino energy of 6.3 petaelectronvolts (PeV) in the rest frame of the electron. Whereas this energy scale is out of reach for currently operating and future planned particle accelerators, natural astrophysical phenomena are expected to produce antineutrinos with energies beyond the PeV scale. Here we report the detection by the IceCube neutrino observatory of a cascade of high-energy particles (a particle shower) consistent with being created at the Glashow resonance. A shower with an energy of 6.05 ± 0.72 PeV (determined from Cherenkov radiation in the Antarctic Ice Sheet) was measured. Features consistent with the production of secondary muons in the particle shower indicate the hadronic decay of a resonant W^- boson, confirm that the source is astrophysical and provide improved directional localization. The evidence of the Glashow resonance suggests the presence of electron antineutrinos in the astrophysical flux, while also providing further validation of the standard model of particle physics. Its unique signature indicates a method of distinguishing neutrinos from antineutrinos, thus providing a way to identify astronomical accelerators that produce neutrinos via hadronuclear or photohadronic interactions, with or without strong magnetic fields. As such, knowledge of both the flavour (that is, electron, muon or tau neutrinos) and charge (neutrino or antineutrino) will facilitate the advancement of neutrino astronomy.

In this Article we present a search for very-high-energy astrophysical neutrinos with IceCube. One event was found with a visible energy of 6.05 ± 0.72 PeV. Given its energy and direction, it is classified as an astrophysical neutrino at the 5σ level. Furthermore, data collected by the sensors closest to the interaction point, as well as the measured energy, are consistent with the hadronic decay of a W^- boson produced on the Glashow resonance. Taking into account only the detector's energy resolution, the probability that the event is produced off-resonance by deep inelastic scattering is 0.01 assuming the best-fit flux from ref.². The neutrino energy is inferred to be about 6.3 PeV by correcting the visible energy for shower particles that do not radiate.

Neutrinos are fundamental particles that couple to matter only via W^\pm or Z^0 boson exchange. As such, they are uniquely suitable messengers to study high-energy particle accelerators in the Universe because they can escape dense media surrounding the production region without interaction and travel to Earth without being deflected by magnetic fields. In the interaction of electron antineutrinos ($\bar{\nu}_e$) with electrons, the standard model predicts the s-channel production of a W^- boson. For a centre-of-mass energy $\sqrt{s} = M_W = 80.38$ GeV (the mass of the W^-), the cross-section becomes resonantly enhanced¹. The standard model cross-section, $\sigma(s)$, for the process $\bar{\nu}_e + e^- \rightarrow W^- \rightarrow X$ is:

$$\sigma(s) = 24\pi\Gamma_W^2 B_{W^- \rightarrow \bar{\nu}_e e^-} \frac{s/M_W^2}{(s - M_W^2)^2 + \Gamma_W^2 M_W^2} \quad (1)$$

where $\Gamma_W = 2.09$ GeV is the W^- decay width and $B_{W^- \rightarrow \bar{\nu}_e e^-}$ its branching ratio for the indicated channel^{3,4}. It is clear from equation (1) that $\sigma(s)$ is maximal when $s = M_W^2$. In the electron (mass $m_e = 0.511$ MeV) rest frame, the resonance energy is $E_R = M_W^2/(2m_e) = 6.32$ PeV.

The resonance energy lies beyond the reach of terrestrial accelerators, but not astrophysical sources of neutrinos. Additionally, since the Glashow resonance is expected to occur for $\bar{\nu}_e$, it is a unique probe of the production mechanism. Neutrinos are expected to be produced in the interaction of high-energy cosmic rays (typically protons) with matter or ambient radiation. In the simplest proton–photon ($p\gamma$) interaction source model, without multi-pion production, the ratio $\bar{\nu}_e : \nu_e = 1 : 3.5$ at Earth³. If, however, there is also a strong magnetic field, $B \geq (0.033 \text{ T}) \times \eta/(1+z)$, where z is redshift and η is the Lorentz boost of the source, synchrotron losses start to dominate over muon decay. This prevents the creation of $\bar{\nu}_e$, which results in a near-zero $\bar{\nu}_e : \nu_e$ ratio at Earth^{3,5}. In the proton–proton (pp) interaction source model, in which cosmic rays interact with the background gas to generate an approximately equal mixture of π^0 , π^- and π^+ , one expects the ratio $\bar{\nu}_e : \nu_e = 1 : 1$ at Earth. A statistically significant measurement of the Glashow resonance event rate thus directly probes the antineutrino fraction and helps to constrain the neutrino production mechanism(s).

As the flux of astrophysical neutrinos drops off following a power law in energy⁶ and its intensity is bounded by cosmic-ray observations⁷, a large-volume detector is needed to detect PeV neutrinos. The IceCube neutrino observatory, situated at the geographic South

*A list of authors and their affiliations appears at the end of the paper.

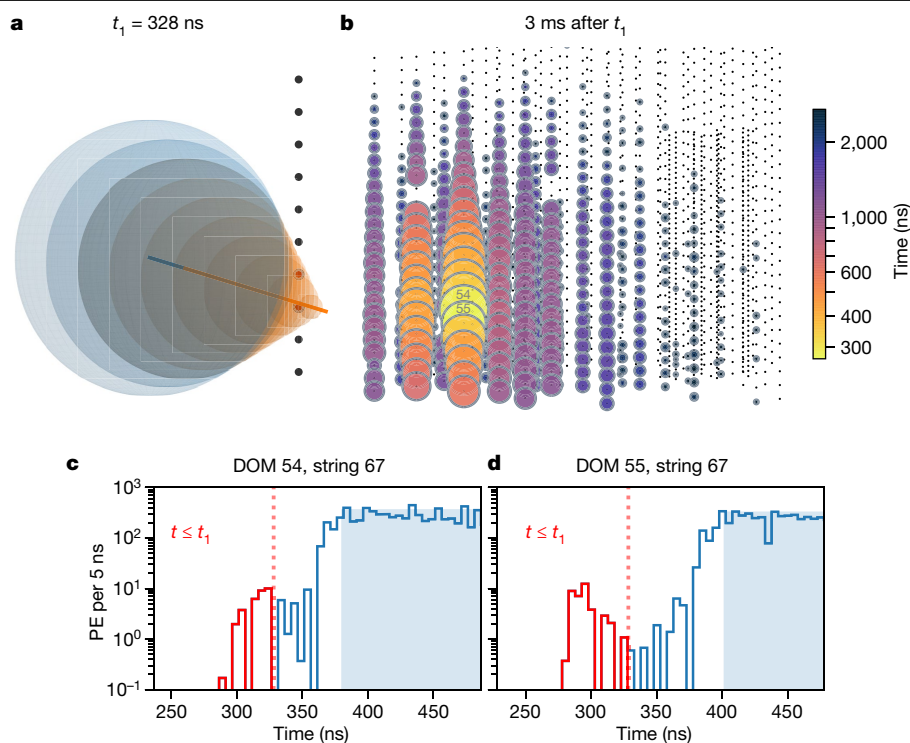


Fig. 1 | Visualization of detected photons at different times and distribution of early pulses. **a**, Schematic of an escaping muon travelling at faster than the speed of light (in ice) and its Cherenkov cone (orange). The muons reach the nearest modules (DOMs 54 and 55 on string 67) ahead of the Cherenkov photons produced by the EM component of the hadronic shower (blue) as these travel at the speed of light in ice. The blue line is associated with the average distance travelled by the main shower, while the orange line extends further and is associated with the muons. Each black dot arranged vertically is a DOM on the nearest string, with the two (slightly larger) dots inside the orange cone the first two to observe early pulses. The time t_1 indicates the approximate time elapsed since the neutrino interaction at which this snapshot graphic was taken. **b**, Event view, showing DOMs that triggered across IceCube at a later time. Each bubble represents a DOM, with its size proportional to the deposited charge. Colours indicate the time each DOM first triggered, relative to our best knowledge of when the initial interaction occurred. The small black dots are DOMs further away that did not detect photons 3 ms after t_1 . **c**, **d**, Distributions of the deposited charge over time on the two earliest hit DOMs, 54 (**c**) and 55 (**d**). The dotted red line is at $t_1 = 328$ ns, the instant shown in **a**. The histogram in red (blue) shows photons arriving before (after) t_1 , and the blue shaded region denotes saturation of the photomultiplier tube.

Pole, instruments a cubic kilometre of ice 1,450–2,450 m beneath the surface⁸—a natural detection medium. It has measured the flux of neutrinos between 10 GeV and 10 PeV, and is sensitive to neutrinos beyond 1 EeV. As neutrinos are uncharged, they are detected in IceCube by the Cherenkov radiation from secondary charged particles produced by their interactions. Cherenkov light collected by digital optical modules (DOMs) is used to reconstruct properties such as the visible energy and incoming direction of the primary neutrino^{9,10}. The visible energy is defined as the energy required of an electromagnetic (EM) shower to produce the light yield observed. As it has no magnet, IceCube cannot distinguish between neutrino and antineutrino interactions on the basis of the charge of the outgoing lepton—whether neutrinos are Dirac or Majorana particles (the latter implying that they are their own antiparticles) remains unresolved. However, owing to the good timing resolution (about 2 ns) of the DOMs^{11,12}, the structure of waveforms recorded by individual modules may contain additional information on the event¹³.

A machine-learning-based algorithm was run to obtain a sample of PeV energy partially contained events (PEPEs)¹⁴. By selecting events near the edge of the detector, the detection volume is increased compared to previous analyses that rely on a smaller, central fiducial volume. Data from May 2012 to May 2017, corresponding to a total live-time of 4.6 years, were analysed. One event was detected on 2016 December 8 at 01:47:59 UTC with visible energy greater than 4 PeV, which is an energy threshold well below the resonance energy and chosen a posteriori in order to study this particular event. The event is shown in Fig. 1, with a reconstructed vertex approximately 80 m from the nearest DOM. The same event was also found in the 9-year extremely high energy search¹⁵. Accounting for systematic uncertainties in photon propagation due to the ice model—a parameterization of the scattering and absorption lengths of light in the ice¹⁶—and the overall detector calibration, the visible energy of the event is 6.05 ± 0.72 PeV. This is consistent with a 6.3-PeV W^- that decays hadronically, since roughly 5% of that energy is expected to be taken by particles that do not emit detectable Cherenkov radiation¹⁰. The boosted decision tree (BDT) classification score is well above the signal threshold, and a posteriori studies of this event, discussed below, lead us to conclude that the event is very likely to be of astrophysical origin.

The main shower was reconstructed by repeating Monte Carlo (MC) simulations under different parameters to find the best-fit energy, vertex and direction⁹. By varying the ice model used in the reconstruction, detector systematic uncertainties on the visible energy, direction and vertex position of the shower were evaluated. Additionally, a global energy scale uncertainty associated with the overall detector calibration was applied to the energy reconstruction.

After reconstruction, three of the DOMs closest to the reconstructed vertex were found to have detected pulses earlier than is possible for photons travelling in ice at $v = 2.19 \times 10^8$ m s⁻¹. Such pulses can, however, be produced by muons created from meson decays in the hadronic shower, which travel close to the speed of light in vacuum ($c = 3.00 \times 10^8$ m s⁻¹). These muons outrun the Cherenkov wavefront of the main shower (by about 1.23 ns per m) while producing Cherenkov radiation near the DOMs, thus depositing early pulses in them, as illustrated in Fig. 1a.

A second reconstruction using only the early pulses to fit a track hypothesis further improves and verifies the directional reconstruction of this event. The two reconstructed directions agree within uncertainties, as shown in Fig. 2. This indicates that the muons and the hadronic shower travel along the same general direction, as is expected from relativistic kinematics. On the basis of the observation that early pulses occurred only on the nearest string, a most-probable leading muon energy of $26.4^{+28.6}_{-12.4}$ GeV was obtained. This is consistent with a distribution of leading muon energies from MC simulations of a 6.3-PeV hadronic shower, which has quartiles of (20, 37, 72) GeV.

Information from both reconstructions refines the estimate of expected backgrounds compared to the sample average. The only possibility for a cosmic-ray-induced atmospheric muon to produce both a 6-PeV cascade and early pulses, as in this event, is for it to reach IceCube at PeV energies and deposit nearly all its energy over a few metres. As a conservative estimate, this background rate was evaluated by considering all atmospheric muons that intersect a cylinder centred on IceCube with radius 800 m and height 1,600 m. By then requiring that muons deposit a visible energy similar to that of the cascade over a short distance, but retain the energy allowed by early pulses, the

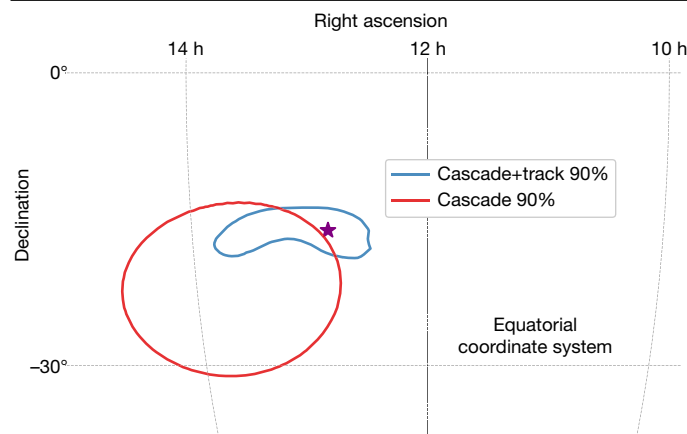


Fig. 2 | Directional reconstructions under two hypotheses. The 90% contours from the cascade (red) and hybrid cascade+track (blue) directional reconstructions are shown in equatorial coordinates. The most-probable direction according to the hybrid reconstruction is shown as the purple star. Systematic uncertainties on the scattering and absorption of photons in ice have been included in both contours. The results are consistent and indicate a common origin. The hybrid reconstruction improves pointing, reducing the contour area by a factor of 5, and should be beneficial to the multi-messenger campaign for such events in the future. Effects of ice anisotropy are shown in the Methods section, and the combined best-fit direction is at right ascension (RA) 12 h 50 min 47.9 s and declination (dec.) -15.9° . The area within the 90% probability cascade+track contour is about 68 deg^2 .

background muon flux is further reduced to give an expectation rate of 1.1×10^{-7} events in 4.6 years. This allows an a posteriori rejection of the cosmic-ray muon background hypothesis by over 5σ .

Similarly, the early pulse signature can be used to reject the atmospheric neutrino background hypothesis. Above roughly 100 TeV, the atmospheric neutrino flux from the prompt decay of charmed mesons is expected to be greater than that from the decay of longer-lived pions and kaons. Charmed mesons can decay to electron (anti)neutrinos that are often accompanied by muons produced in other branches of the same air shower. These muons can be used to veto atmospheric neutrinos^{17,18}. The expectation rate of atmospheric neutrinos passing the PEPE event selection with accompanying muon energy consistent with the observed early pulses is around 2×10^{-7} in 4.6 years. We conclude that the event is induced by an astrophysical neutrino.

Given the negligible atmospheric background rate, the remainder of this Article assumes that the event originated from a single high-energy astrophysical neutrino interaction. The major backgrounds to the Glashow resonance are charged-current (CC) interactions (mediated by the exchange of a virtual W^\pm) of electron (anti) neutrinos with nucleons. Neutral-current (NC) interactions (mediated by the exchange of a virtual Z^0) from all three flavours are a secondary background. Figure 3b illustrates the expected rate from each interaction channel. The posterior distribution of visible energy, reconstructed assuming a cascade hypothesis for different ice models, has a 68% highest-probability-density region of $6.05 \pm 0.72 \text{ PeV}$ and is shown in Fig. 3a. Assuming a single power-law astrophysical flux with $\bar{\nu} : \nu = 1 : 1$, astrophysical spectral index $\gamma_{\text{astro}} = 2.49$ and normalization at 100 TeV of $2.33 \times 10^{-18} \text{ GeV}^{-1} \text{ cm}^{-2} \text{ s}^{-1} \text{ sr}^{-1}$ (ref. ²), we expect to observe 1.55 Glashow resonance hadronic cascades in our data.

Assuming the best-fit flux in ref. ², a likelihood-ratio test based on the visible energy rejects both CC and NC interactions in favour of Glashow resonance with a P value of 0.01, corresponding to a (one-sided) significance of 2.3σ . Systematic uncertainties due to the ice modelling and the global energy scale, which affect the visible energy reconstruction, are included. The P value is also tested against spectral assumptions under a single power-law flux, and the results for other spectra are

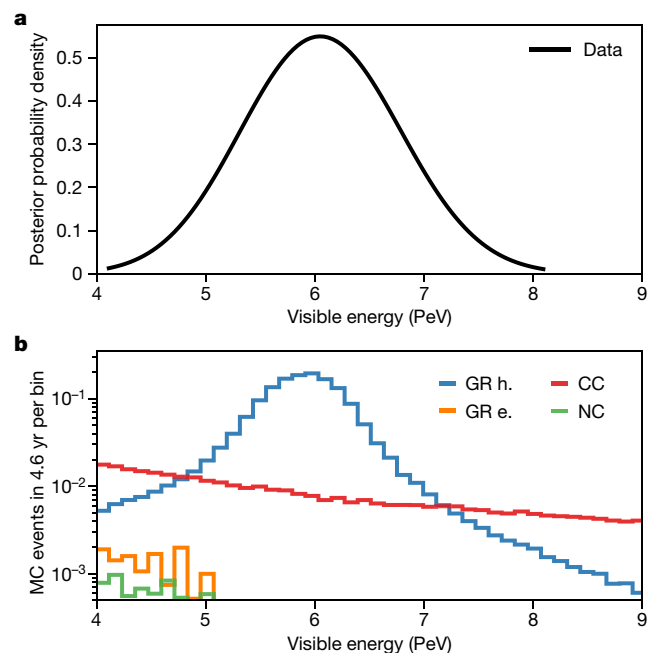


Fig. 3 | Reconstructed energy posterior probability density and expected distributions from MC simulations. **a**, Posterior probability density of the visible energy for this event. Systematic uncertainties due to the ice and global energy scale of the detector are included. **b**, Expected Monte Carlo (MC) event distributions in visible energy of hadrons from W^- decay (GR h., blue), the electron from W^- decay (GR e., orange), charged-current interactions (CC; red) and neutral-current interactions (NC; green) for a live-time of 4.6 years from the PEPE sample. We assume the ratio $\bar{\nu} : \nu = 1 : 1$, a flavour ratio of 1:1:1 at Earth, an astrophysical spectrum measured from ref. ², and cross-sections according to equation (1) and ref. ³². The effect of Doppler broadening on the Glashow resonance (GR)³³ is also taken into account.

given in Methods. The test's sensitivity is due to the fact that the visible energy distribution from Glashow resonance differs both in shape and in normalization from the background at these energies.

This is a conservative estimate that does not rely on early pulses. As muons are produced in meson decay, the energy of the hadronic shower is directly related to the leading muon energy. In electron neutrino CC interaction at these energies, on average only about 20% of the total neutrino energy is deposited hadronically. Thus, while the amount of early Cherenkov light is consistent with the leading muon energy expected from a hadronic shower at the Glashow resonance (6.3 PeV), it is an order of magnitude above that expected from a CC electron neutrino interaction at those energies. In NC interactions, the outgoing neutrino escapes undetected and carries away a large portion of the total energy. Thus, while an NC shower is purely hadronic, a much higher incoming neutrino energy is required. The steeply falling power-law flux of astrophysical neutrinos results in a suppression of the NC background.

Although we would ideally incorporate early pulses for CC and NC background rejection, there are several technical challenges that this can pose, including full resimulations of the MC sets that include systematic uncertainties of the hadronic interaction models. Such studies are under way, and inclusion of this information will be especially important for IceCube-Gen2¹⁹, which, owing to its much larger effective area, will record many more events at the Glashow resonance.

A segmented differential flux fit²⁰ was also performed using three equal-width bins in the logarithm of the neutrino energy over the range 4 PeV to 10 PeV. The results, shown in Fig. 4 (red), complement other IceCube diffuse analyses^{21–24}. The central energy bin extends the

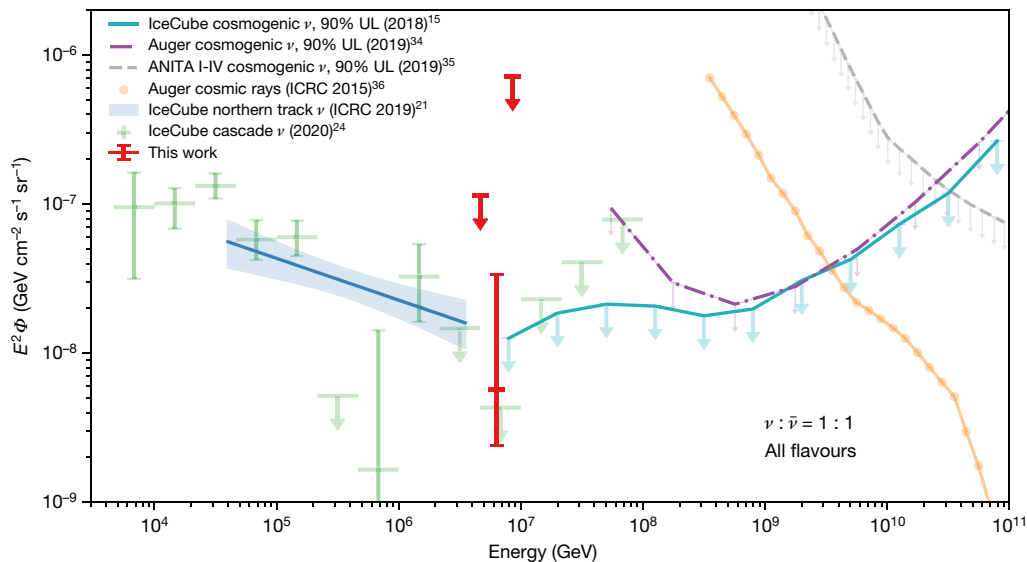


Fig. 4 | Measured flux of astrophysical neutrinos. Global picture of astrophysical neutrino flux measurements^{21,24}, cosmogenic neutrino upper limits (UL)^{15,34,35} and the ultra-high-energy cosmic-ray spectrum³⁶. The y axis is given in terms of the energy, E , squared times the flux, Φ . We assume the ratio $\bar{\nu} : \nu = 1 : 1$, a flavour ratio of 1:1:1 at Earth, an astrophysical spectrum measured

from ref.², and cross-sections according to equation (1) and ref.³². This result extends the measured astrophysical flux to 6.3 PeV. The luminosity densities of high-energy neutrinos and extragalactic ultra-high-energy cosmic rays are found to be comparable.

measurement of the differential neutrino energy spectrum to 6.3 PeV, while 68% upper limits are shown for the lower and upper energy bins. Arguments based on energetics²⁵ and astrophysical unification models^{26–30} suggest a common origin of diffuse γ -rays, high-energy neutrinos and ultra-high-energy cosmic rays. A precise measurement of the cosmic neutrino flux at the Glashow resonance energy would be able to test these predictions, and possibly uncover the origins of ultra-high-energy cosmic rays if the sources can be identified directly via multimessenger observations.

Although the present results focus on just one event, the techniques developed here have implications for the future direction of neutrino astrophysics. For example, the idealized $p\gamma$ muon damped model of neutrino production is already inconsistent with the result presented here of a likely Glashow resonance because such sources produce no electron antineutrinos. With just one event, pp source models cannot be constrained, but the planned IceCube-Gen2 experiment¹⁹ will increase the instrumented volume by an order of magnitude. The statistics collected by such a detector should allow us to differentiate between pp and idealized $p\gamma$ models at a high significance level.

In more realistic source models³¹, multi-pion production in $p\gamma$ sources generates antineutrinos and the $\bar{\nu}_e : \nu_e$ ratio depends on the photon density, the mass composition of cosmic rays and also the magnetic field strength of the source. In such cases, a multi-messenger campaign to detect the sources of future Glashow resonance candidates could help determine their production mechanisms. Using the hybrid (early muon and cascade reconstruction) approach could reduce the angular uncertainty by a factor of about 5, and, as this technique shows, an uncertainty of about 68 deg² at 90% containment is possible for hadronic cascades. In the near future, such techniques would greatly aid searches for multimessenger counterparts in real time.

Online content

Any methods, additional references, Nature Research reporting summaries, source data, extended data, supplementary information, acknowledgements, peer review information; details of author contributions and competing interests; and statements of data and code availability are available at <https://doi.org/10.1038/s41586-021-03256-1>.

- Glashow, S. L. Resonant scattering of antineutrinos. *Phys. Rev.* **118**, 316–317 (1960).
- Mohrmann, L. Update of a combined analysis of the high-energy cosmic neutrino flux at the IceCube detector. In *Proc. 34th Int. Cosmic Ray Conf. (ICRC 2015)* 1066 (Proceedings of Science, 2016).
- Barger, V. et al. Glashow resonance as a window into cosmic neutrino sources. *Phys. Rev. D* **90**, 121301 (2014).
- Zyla, P. A. et al. Review of particle physics. *Prog. Theor. Exp. Phys.* **2020**, 083C01 (2020).
- Kashti, T. & Waxman, E. Flavoring astrophysical neutrinos: flavor ratios depend on energy. *Phys. Rev. Lett.* **95**, 181101 (2005).
- Bell, A. R. The acceleration of cosmic rays in shock fronts. I. *Mon. Not. R. Astron. Soc.* **182**, 147–156 (1978).
- Waxman, E. & Bahcall, J. N. High-energy neutrinos from astrophysical sources: an upper bound. *Phys. Rev. D* **59**, 023002 (1998).
- Aartsen, M. G. et al. The IceCube Neutrino Observatory: instrumentation and online systems. *J. Instrum.* **12**, P03012 (2017).
- Chirkin, D. Event reconstruction in IceCube based on direct event re-simulation. In *Proc. 33rd Int. Cosmic Ray Conf. (ICRC2013)* 0581 (2013).
- Aartsen, M. G. et al. Energy reconstruction methods in the IceCube neutrino telescope. *J. Instrum.* **9**, P03009 (2014).
- Abbasi, R. et al. The IceCube data acquisition system: signal capture, digitization, and timestamping. *Nucl. Instrum. Methods A* **601**, 294–316 (2009).
- Abbasi, R. et al. Calibration and characterization of the IceCube photomultiplier tube. *Nucl. Instrum. Methods A* **618**, 139–152 (2010).
- Aartsen, M. et al. Search for astrophysical tau neutrinos in three years of IceCube data. *Phys. Rev. D* **93**, 022001 (2016).
- Lu, L. Multi-flavour PeV neutrino search with IceCube. In *Proc. 35th Int. Cosmic Ray Conf. (ICRC 2017)* 1002 (Proceedings of Science, 2018).
- Aartsen, M. G. et al. Differential limit on the extremely-high-energy cosmic neutrino flux in the presence of astrophysical background from nine years of IceCube data. *Phys. Rev. D* **98**, 062003 (2018).
- Aartsen, M. G. et al. Measurement of South Pole ice transparency with the IceCube LED calibration system. *Nucl. Instrum. Methods A* **711**, 73–89 (2013).
- Gaisser, T. K., Jero, K., Karle, A. & van Santen, J. Generalized self-veto probability for atmospheric neutrinos. *Phys. Rev. D* **90**, 023009 (2014).
- Argüelles, C. A., Palomares-Ruiz, S., Schneider, A., Wille, L. & Yuan, T. Unified atmospheric neutrino passing fractions for large-scale neutrino telescopes. *J. Cosmol. Astropart. Phys.* **1807**, 047 (2018).
- Aartsen, M. et al. IceCube-Gen2: the window to the extreme Universe. Preprint at <https://arxiv.org/abs/2008.04323> (2020).
- Aartsen, M. G. et al. Observation of high-energy astrophysical neutrinos in three years of IceCube data. *Phys. Rev. Lett.* **113**, 101101 (2014).
- Stettner, J. Measurement of the diffuse astrophysical muon-neutrino spectrum with ten years of IceCube Data. In *Proc. 36th Int. Cosmic Ray Conf. (ICRC2019)* 1017 (Proceedings of Science, 2019).
- Abbasi, R. et al. The IceCube high-energy starting event sample: description and flux characterization with 7.5 years of data. Preprint at <https://arxiv.org/abs/2011.03545> (2020).
- Aartsen, M. et al. Measurements using the inelasticity distribution of multi-TeV neutrino interactions in IceCube. *Phys. Rev. D* **99**, 032004 (2019).
- Aartsen, M. et al. Characteristics of the diffuse astrophysical electron and tau neutrino flux with six years of IceCube high energy cascade data. *Phys. Rev. Lett.* **125**, 121104 (2020).

25. Murase, K. & Fukugita, M. Energetics of high-energy cosmic radiations. *Phys. Rev. D* **99**, 063012 (2019).
 26. Fang, K. & Murase, K. Linking high-energy cosmic particles by black hole jets embedded in large-scale structures. *Nat. Phys.* **14**, 396–398 (2018).
 27. Zhang, B. T., Murase, K., Kimura, S. S., Horiuchi, S. & Mészáros, P. Low-luminosity gamma-ray bursts as the sources of ultrahigh-energy cosmic ray nuclei. *Phys. Rev. D* **97**, 083010 (2018).
 28. Muzio, M. S., Unger, M. & Farrar, G. R. Progress towards characterizing ultrahigh energy cosmic ray sources. *Phys. Rev. D* **100**, 103008 (2019).
 29. Liu, R.-Y., Wang, X.-Y., Inoue, S., Crocker, R. & Aharonian, F. Diffuse PeV neutrinos from EeV cosmic ray sources: semirelativistic hypernova remnants in star-forming galaxies. *Phys. Rev. D* **89**, 083004 (2014).
 30. Boncioli, D., Biehl, D. & Winter, W. On the common origin of cosmic rays across the ankle and diffuse neutrinos at the highest energies from low-luminosity gamma-ray bursts. *Astrophys. J.* **872**, 110 (2019).
 31. Biehl, D., Fedynitch, A., Palladino, A., Weiler, T. J. & Winter, W. Astrophysical neutrino production diagnostics with the Glashow resonance. *J. Cosmol. Astropart. Phys.* **1701**, 033 (2017).
 32. Cooper-Sarkar, A., Mertsch, P. & Sarkar, S. The high energy neutrino cross-section in the Standard Model and its uncertainty. *J. High Energy Phys.* **08**, 042 (2011).
 33. Loewy, A., Nussinov, S. & Glashow, S. L. The effect of Doppler broadening on the 6.3 PeV W^- resonance in $\bar{\nu}_e \bar{e}$ collisions. Preprint at <https://arxiv.org/abs/1407.4415> (2014).
 34. Aab, A. et al. Probing the origin of ultra-high-energy cosmic rays with neutrinos in the EeV energy range using the Pierre Auger Observatory. *J. Cosmol. Astropart. Phys.* **10**, 022 (2019).
 35. Gorham, P. et al. Constraints on the ultrahigh-energy cosmic neutrino flux from the fourth flight of ANITA. *Phys. Rev. D* **99**, 122001 (2019).
 36. Valino, I. The flux of ultra-high energy cosmic rays after ten years of operation of the Pierre Auger Observatory. In *Proc. 34th Int. Cosmic Ray Conf. (ICRC 2015) 271* (Proceedings of Science, 2016).
- Publisher's note** Springer Nature remains neutral with regard to jurisdictional claims in published maps and institutional affiliations.
- © The Author(s), under exclusive licence to Springer Nature Limited 2021, corrected publication 2021
-
- The IceCube Collaboration** 
- M. G. Aartsen¹, R. Abbasi², M. Ackermann³, J. Adams⁴, J. A. Aguilar⁴, M. Ahlers⁵, M. Ahrens⁶, C. Alispach⁷, N. M. Amin⁸, K. Andeen⁹, T. Anderson¹⁰, I. Ansseau¹¹, G. Anton¹², C. Argüelles¹², J. Auffenberg¹³, S. Axani¹⁴, H. Bagherpour¹⁵, X. Bai¹⁵, A. Balagopal V.¹⁶, A. Barbano⁷, S. W. Barwick¹⁷, B. Bastian¹⁸, V. Basu¹⁹, V. Baum¹⁹, S. Baur⁴, R. Bay²⁰, J. J. Beatty^{21,22}, K.-H. Becker²³, J. Becker Tjus²⁴, C. Bellenghi²⁵, S. BenZvi²⁶, D. Berley²⁷, E. Bernardini^{13,28}, D. Z. Besson^{29,30}, G. Binder^{30,31}, D. Bindig²³, E. Blaufuss²⁷, S. Blot³, C. Boehm⁶, S. Böser¹⁹, O. Botner³², J. Böttcher¹³, E. Bourbeau³³, J. Bourbeau¹⁹, F. Bradascio³, J. Braun¹⁸, S. Bron⁷, J. Brosteanu-Kaiser³, A. Burgman³², J. Buscher¹³, R. S. Busse³³, M. A. Campana³⁴, T. Carver⁷, C. Chen³⁵, E. Cheung²⁷, D. Chirkin¹⁸, S. Choi³⁶, B. A. Clark³⁷, K. Clark³⁸, L. Classen³³, A. Coleman⁸, G. H. Collin¹⁴, J. M. Conrad¹⁴, P. Coppin³⁹, P. Correa³⁹, D. F. Cowen^{10,40}, R. Cross²⁶, P. Dave³⁵, C. De Clercq³⁹, J. J. DeLaunay¹⁰, H. Dembinski⁸, K. Deoskar⁶, S. De Ridder⁴¹, A. Desai¹⁸, P. Desiati¹⁸, K. D. de Vries³⁹, G. de Wasseige³⁹, M. de With⁴², T. DeYoung³⁷, S. Dharani¹³, A. Diaz⁴⁴, J. C. Díaz-Vélez¹⁸, H. Dujmovic¹⁶, M. Dunkman¹⁰, M. A. DuVernois¹⁸, E. Dvorak¹⁵, T. Ehrhardt¹⁹, P. Eller¹⁶, R. Engel¹⁶, P. A. Evenson⁸, S. Fahey¹⁸, A. R. Fazely⁴³, A. Fedynitch^{3,44}, J. Felde²⁷, A. T. Fienberg¹⁰, K. Filimonov²⁰, C. Finley⁶, L. Fischer³, D. Fox⁴⁰, A. Franczkowiak⁷, E. Friedman²⁷, A. Fritz¹⁰, T. K. Gaisser⁸, J. Gallagher¹⁵, E. Ganster¹³, S. Garrappa³, L. Gerhardt³¹, A. Ghadimi⁴⁶, T. Glauch²⁵, T. Glüsenkamp¹¹, A. Goldschmidt³¹, J. G. Gonzalez⁸, S. Goswami⁴⁶, D. Grant³⁷, T. Grégoire¹⁰, Z. Griffith¹⁸, S. Griswold²⁶, M. Gündüz²⁴, C. Haack¹³, A. Hallgren²², R. Halliday²⁷, L. Halve¹³, F. Halzen^{18,51}, K. Hanson¹⁸, J. Hardin¹⁸, A. Haungs¹⁶, S. Hauser¹³, D. Hebecker⁴², P. Heix¹³, K. Helbing²³, R. Hellauer²⁷, F. Henningsen²⁵, S. Hickford²³, J. Hignight⁴⁷, G. C. Hill⁴⁸, G. C. Hill⁴⁹, K. D. Hoffman²⁷, R. Hoffmann²⁷, T. Hoinka⁵⁰, B. Hokanson-Fasig³, K. Hoshina^{18,51}, F. Huang¹⁰, M. Huber²⁵, T. Huber¹⁶, K. Hultqvist⁶, M. Hünnefeld⁵⁰, R. Hussain¹⁸, S. In³⁶, N. Iovine⁴, A. Ishihara⁴⁸, M. Jansson⁶, S. Japaridze⁵², M. Jeong³⁶, B. J. P. Jones⁵³, F. Jonske¹³, R. Joppe¹³, D. Kang¹⁶, W. Kang³⁶, X. Kang³⁴, A. Kappes³³, D. Kappesser¹⁹, T. Karg³, M. Karl²⁵, A. Karle¹⁶, U. Katz¹¹, M. Kauer¹⁸, M. Kellermann¹³, J. L. Kelley¹⁸, A. Kheirandish¹⁰, J. Kim³⁶, K. Kin⁴⁸, T. Kintscher³, J. Kiryluk⁵⁴, T. Kitter¹¹, S. R. Klein^{20,31}, R. Koirala⁸, H. Kolanoski⁴², L. Köpke¹⁹, C. Kopper³⁷, S. Kopper⁴⁶, D. J. Koskinen¹⁹, P. Koundal¹⁶, M. Kovacevich³⁴, M. Kowalski^{3,42}, K. Krings²⁵, G. Krück¹⁹, N. Kulacz⁴⁷, N. Kurahashi³⁴, A. Kyriacou⁴⁹, C. Lagunas Gualda³, J. L. Lanfranchi¹⁰, M. J. Larson²⁷, F. Lauber²³, J. P. Lazar^{12,18}, K. Leonard¹⁸, A. Leszczyńska¹⁶, Y. Li¹⁰, Q. R. Liu¹⁸, E. Lohfink¹⁹, C. J. Lozano Mariscal³³, L. Lu⁴⁶, F. Lucarelli¹, A. Ludwig⁵⁵, J. Lünemann³⁹, W. Luszczak¹⁸, Y. Lyu^{20,31}, W. Y. Ma³, J. Madsen¹⁸, G. Maggi³⁹, K. B. M. Mahn³⁷, Y. Makino¹⁸, P. Mallik¹³, S. Mancina¹⁸, I. C. Maric⁴, R. Maruyama⁵⁶, K. Mase⁴⁸, R. Maunu²⁷, F. McNally⁵⁷, K. Meagher¹⁸, M. Medici⁴, A. Medina²², M. Meier⁴⁹, S. Meighen-Berger²⁵, J. Merz¹³, J. Micallef²⁷, D. Mockler⁴, G. Momente¹⁹, T. Montaruli⁷, R. W. Moore⁴⁷, R. Morse¹⁸, M. Moulai⁴, P. Muth¹³, R. Naab³, R. Nagai⁴⁸, U. Naumann²³, J. Necker³, G. Neer³⁷, L. V. Nguyen³⁷, H. Niederhausen²⁵, M. U. Nisa³⁷, S. C. Nowicki¹⁷, D. R. Nygren³¹, A. Obertacke Pollmann²³, M. Oehler¹⁶, A. Olivas²⁷, E. O'Sullivan²⁷, H. Pandya⁸, D. V. Pankova¹⁰, N. Park¹⁸, G. K. Parker⁵³, E. N. Paudel⁸, P. Peiffer¹⁹, C. Pérez de los Heros³², S. Philippen¹³, D. Pieloth⁵⁰, S. Pieper²³, A. Pizzuto¹⁸, M. Plum⁹, Y. Popovych¹³, A. Porcelli⁴¹, M. Prado Rodriguez²⁸, P. B. Price²⁰, G. T. Przybylski²¹, C. Raab⁴, A. Raissi¹, M. Rameez², L. Rauch³, K. Rawlins⁵⁸, I. C. Rea²⁵, A. Rehman⁹, R. Reimann¹³, M. Relich⁴⁸, M. Renschler¹⁶, G. Renzi⁴, E. Resconi²⁵, S. Reusch³, W. Rhode⁵⁰, M. Richman³⁴, B. Riedel¹⁸, S. Robertson^{20,31}, G. Roellinghoff³⁶, M. Rongen¹³, C. Rott²⁰, T. Ruhe⁵⁰, D. Ryckbosch⁴¹, D. Rysewyk Cantu³⁷, I. Safa^{12,18}, S. E. Sanchez Herrera³⁷, A. Sandrock⁵⁰, J. Sandroos¹⁹, M. Santander⁴⁶, S. Sarkar⁵⁹, S. Sarkar⁴⁷, K. Satalecka³, M. Scharf¹³, M. Schaufel¹³, H. Schieler¹⁶, P. Schlunder⁵⁰, T. Schmidt²⁷, A. Schneider¹⁸, J. Schneider¹¹, F. G. Schröder^{51,16}, L. Schumacher¹³, S. Sclafani³⁴, D. Seckel⁶, S. Seunarine⁶⁰, S. Shefali¹³, M. Silva¹⁶, B. Smithers⁵³, R. Snihur¹⁸, J. Soedingrekso⁵⁰, D. Soldin⁸, M. Song²⁷, G. M. Spiczak⁶⁰, C. Spiering^{3,30}, J. Stachurska³, M. Stamatikos²², T. Stanev⁸, R. Stein³, J. Stettner¹³, A. Steuer¹⁹, T. Stezelberger³¹, R. G. Stokstad³¹, N. L. Strotjohann³, T. Stürwald¹³, T. Stuttard⁵, G. W. Sullivan²⁷, I. Taboada³⁵, F. Tenholt²⁴, S. Ter-Antonyan⁴³, A. Terliuk³, S. Tilav⁸, K. Tollefson³⁷, L. Tomankova²⁴, C. Tönnis⁶¹, S. Toscano⁴, D. Tosi¹⁸, A. Trettin³, M. Tselengidou¹³, C. F. Tung³⁵, A. Turcati²⁵, R. Turcotte¹⁶, C. F. Turley¹⁰, J. P. Twagirayezu³⁷, B. Ty¹⁸, E. Unger³², M. A. Unland Elorrieta³³, J. Vandenbroucke¹⁸, D. van Eijk¹⁸, N. van Eijndhoven³⁹, D. Vannerom¹⁴, J. van Santen³, S. Verpoest⁴¹, M. Vraeghe⁴¹, C. Walck⁶, A. Wallace⁴⁹, N. Wandkowsky¹⁸, T. B. Watson⁵³, C. Weaver⁴⁷, A. Weindl¹⁶, M. J. Wiebe¹⁰, J. Weldert¹⁹, C. Wendt¹⁸, J. Werthebach⁵⁰, B. J. Whelan⁴⁹, N. Whitehorn^{37,55}, K. Wiebe¹⁹, C. H. Wiebusch¹³, D. R. Williams⁴⁶, M. Wolf²⁵, T. R. Wood⁴⁷, K. Woschnagg²⁰, G. Wrede¹¹, J. Wulff²⁴, X. W. Xu⁴³, Y. Xu⁵⁴, J. P. Yanez⁴⁷, S. Yoshida⁴⁸, T. Yuan¹⁸, Z. Zhang⁵⁴ & M. Zöcklein¹³

¹Department of Physics and Astronomy, University of Canterbury, Christchurch, New Zealand. ²Department of Physics, Loyola University Chicago, Chicago, IL, USA. ³DESY, Zeuthen, Germany. ⁴Science Faculty, Université Libre de Bruxelles, Brussels, Belgium. ⁵Niels Bohr Institute, University of Copenhagen, Copenhagen, Denmark. ⁶Oskar Klein Centre and Department of Physics, Stockholm University, Stockholm, Sweden. ⁷Département de Physique Nucléaire et Corpusculaire, Université de Genève, Geneva, Switzerland. ⁸Bartol Research Institute and Department of Physics and Astronomy, University of Delaware, Newark, DE, USA. ⁹Department of Physics, Marquette University, Milwaukee, WI, USA. ¹⁰Department of Physics, Pennsylvania State University, University Park, PA, USA. ¹¹Erlangen Centre for Astroparticle Physics, Friedrich-Alexander-Universität Erlangen-Nürnberg, Erlangen, Germany. ¹²Department of Physics and Laboratory for Particle Physics and Cosmology, Harvard University, Cambridge, MA, USA. ¹³III. Physikalisches Institut, RWTH Aachen University, Aachen, Germany. ¹⁴Department of Physics, Massachusetts Institute of Technology, Cambridge, MA, USA. ¹⁵Physics Department, South Dakota School of Mines and Technology, Rapid City, SD, USA. ¹⁶Karlsruhe Institute of Technology, Institute for Astroparticle Physics, Karlsruhe, Germany. ¹⁷Department of Physics and Astronomy, University of California, Irvine, CA, USA. ¹⁸Department of Physics and Wisconsin IceCube Particle Astrophysics Center, University of Wisconsin–Madison, Madison, WI, USA. ¹⁹Institute of Physics, University of Mainz, Mainz, Germany. ²⁰Department of Physics, University of California, Berkeley, CA, USA. ²¹Department of Astronomy, Ohio State University, Columbus, OH, USA. ²²Department of Physics and Center for Cosmology and AstroParticle Physics, Ohio State University, Columbus, OH, USA. ²³Department of Physics, University of Wuppertal, Wuppertal, Germany. ²⁴Fakultät für Physik und Astronomie, Ruhr-Universität Bochum, Bochum, Germany. ²⁵Physik-Department, Technische Universität München, Garching, Germany. ²⁶Department of Physics and Astronomy, University of Rochester, Rochester, NY, USA. ²⁷Department of Physics, University of Maryland, College Park, MD, USA. ²⁸Università di Padova, Padua, Italy. ²⁹Department of Physics and Astronomy, University of Kansas, Lawrence, KS, USA. ³⁰National Research Nuclear University, Moscow Engineering Physics Institute (MEPhI), Moscow, Russia. ³¹Lawrence Berkeley National Laboratory, Berkeley, CA, USA. ³²Department of Physics and Astronomy, Uppsala University, Uppsala, Sweden. ³³Institut für Kernphysik, Westfälische Wilhelms-Universität Münster, Münster, Germany. ³⁴Department of Physics, Drexel University, Philadelphia, PA, USA. ³⁵School of Physics and Center for Relativistic Astrophysics, Georgia Institute of Technology, Atlanta, GA, USA. ³⁶Department of Physics, Sungkyunkwan University, Suwon, Korea. ³⁷Department of Physics and Astronomy, Michigan State University, East Lansing, MI, USA. ³⁸SNOLAB, Lively, Ontario, Canada. ³⁹Vrije Universiteit Brussel (VUB), Dienst ELEM, Brussels, Belgium. ⁴⁰Department of Astronomy and Astrophysics, Pennsylvania State University, University Park, PA, USA. ⁴¹Department of Physics and Astronomy, University of Ghent, Ghent, Belgium. ⁴²Institut für Physik, Humboldt-Universität zu Berlin, Berlin, Germany. ⁴³Department of Physics, Southern University, Baton Rouge, LA, USA. ⁴⁴Institute for Cosmic Ray Research, University of Tokyo, Kashiwa, Japan. ⁴⁵Department of Astronomy, University of Wisconsin–Madison, Madison, WI, USA. ⁴⁶Department of Physics and Astronomy, University of Alabama, Tuscaloosa, AL, USA. ⁴⁷Department of Physics, University of Alberta, Edmonton, Alberta, Canada. ⁴⁸Department of Physics and Institute for Global Prominent Research, Chiba University, Chiba, Japan. ⁴⁹Department of Physics, University of Adelaide, Adelaide, South Australia, Australia. ⁵⁰Department of Physics, TU Dortmund University, Dortmund, Germany. ⁵¹Earthquake Research Institute, University of Tokyo, Tokyo, Japan. ⁵²CTSPS, Clark-Atlanta University, Atlanta, GA, USA. ⁵³Department of Physics, University of Texas at Arlington, Arlington, TX, USA. ⁵⁴Department of Physics and Astronomy, Stony Brook University, Stony Brook, NY, USA. ⁵⁵Department of Physics and Astronomy, University of California, Los Angeles, CA, USA. ⁵⁶Department of Physics, Yale University, New Haven, CT, USA. ⁵⁷Department of Physics, Mercer University, Macon, GA, USA. ⁵⁸Department of Physics and Astronomy, University of Alaska Anchorage, Anchorage, AK, USA. ⁵⁹Department of Physics, University of Oxford, Oxford, UK. ⁶⁰Department of Physics, University of Wisconsin, River Falls, WI, USA. ⁶¹Institute of Basic Science, Sungkyunkwan University, Suwon, Korea. ⁵²e-mail: analysis@icecube.wisc.edu

Methods

Detection principles

IceCube instruments a cubic kilometre of Antarctic ice with 5,160 DOMs, each containing a single downward-facing photomultiplier tube (PMT). The DOMs are placed on 86 strings that extend from 1,450 m to 2,450 m beneath the surface⁸. Charged particles travelling above the group velocity of light in ice (velocity $v > 0.73c$) emit light, which is detectable by the PMTs. When multiple groups of PMTs detect photons within a window of 5 μ s, the recorded charges are digitized and saved as an “event”⁸.

IceCube events are typically classified into two different categories depending on the outgoing secondaries. High-energy muons that start in or travel through the detector are classified as tracks. Such muons are created in CC interactions of incoming muon neutrinos. Hadronic and EM showers have shorter extension (about 10 m) and are classified as cascades. These can arise either from CC interactions of incoming electron and tau neutrinos, or, with smaller probability, NC interactions of all three neutrino flavours. In some cases, tau neutrino CC interactions can produce more complicated event signatures³⁷.

Additionally, an interaction via the Glashow resonance can produce a characteristic event type and energy deposition in IceCube. A W^- decays to hadrons 67.41% of the time. In such cases, the visible energy is lower than the total energy of all particles in the shower, as there is a substantial fraction of neutral particles and particles with higher energy thresholds to produce Cherenkov radiation¹⁰. Based on the known properties of the resonance peak—both M_W and the relatively narrow width, Γ_W —the resulting hadronic shower is expected to deposit about 6.0 PeV visible energy. Low-energy muons are expected to be produced in and outrun the Cherenkov wavefront of the shower at a rate high enough to potentially trigger early pulses. In the leptonic channel, the W^- decays to an antineutrino and a charged lepton with a branching ratio to each flavour of about 11%. As the antineutrino escapes undetected, a varying fraction of the primary energy is visible as a muon track, EM cascade, or tau. This signature is uniquely lacking a hadronic component. However, with the wider range of possible charged-lepton energies, it is difficult to distinguish the leptonic channel from CC or NC background without more sophisticated tagging techniques.

Event selection

IceCube discovered astrophysical neutrinos using high-energy starting events (HESE) with interaction vertices inside a restricted fiducial region^{38,39}. These events were selected with a veto-based approach, with the outer layer of the detector used to reject the large muon background. The highest-visible-energy cascade detected by HESE was an event of about 2 PeV (ref. ²⁰). To enhance the detection rate of Glashow resonance events, a larger fiducial volume is required. The PEPE selection aims to select multi-PeV, cascade-like events with interaction vertices near the edge of the detector. It preferentially selects cascades because of their higher energy resolution compared to that of tracks¹⁴. At the Glashow resonance, the event rate is about twice that of the HESE selection³⁹, as shown in Extended Data Table 1. The PEPE background is dominated by cosmic-ray muons propagating through corners of the detector that appear cascade-like.

First, events with a total charge of less than 1,000 photoelectrons or involving fewer than 15 sensors with charge ≥ 5 photoelectrons are rejected to ensure a minimum level of detectable light deposited in the detector to be used in reconstructions. Second, events seen previously in the HESE sample³⁹ and tracks in the online extremely high-energy alerts sample¹⁵ are removed. In addition, events where a single sensor carries more than 50% of total charge tend to be more difficult to reconstruct and are also excluded. Last, to constrain the vertex to be located at the edge of the detector, cumulative charges on the outer two strings are required to be at least 80% of the total charge. After these cuts, the cosmic-ray background rate is about 0.05 Hz.

To further reject tracks, a BDT was trained against a background of atmospheric muons, with the signals being ν_e and $\bar{\nu}_e$ of neutrino energy 1–10 PeV. In total, 11 features are selected for training as follows: the charge of the event, the number of triggered sensors above 5 photoelectrons, the centre of charge (which describes the location of the event) and its projection onto the x – y plane, the travel of the centre of charge relative to the first quartile in time and its projections onto the z axis and the x – y plane, the ratio of the travel along the z axis to the total number of DOMs, the goodness of fit for a track hypothesis, the time between the first hit overall and the first hit on the sensor with the largest total charge, and the cumulative fraction of total charge at 600 ns from the start of the event. These parameters summarize the difference between tracks and cascades. The charge of the event serves as a proxy for the energy. Extended Data Fig. 1 shows the BDT score distribution for events with a reconstructed energy above 4 PeV. The final selection includes only events with a BDT score above 0.5 that fit well under a cascade hypothesis¹⁰. With this, the cosmic-ray background for reconstructed energy ≥ 4 PeV is about 0.02 events per year. The BDT score of the event discussed in this work is 0.65.

Nine events passed all selection criteria, with this event the only one having energy above 4 PeV. The remaining events all had energies below 2 PeV and will be discussed in a future publication. The effective area, defined as the ratio of the event rate to the flux, near the Glashow resonance energy is increased by a factor of about 2 compared to HESE³⁹. For 4.6 years of data-taking, with the most recent global-fit spectrum², 1.55 (0.69) PEPE events are expected in the hadronic channel of W -decay from Glashow resonance assuming pp ($p\bar{p}$) interactions. However, it is worth noting that a spectral cutoff can substantially change the number of expected PEPE events¹⁴.

Reconstruction

The event reported in this Article is reconstructed in a two-step process using Bayesian techniques: first, to reconstruct the visible energy, interaction vertex, and direction of the initial cascade⁹, and second, to reconstruct the direction more precisely using early pulses, with a prior on the interaction vertex⁴⁰. These two steps rely on independent information, as the early pulses occur on DOMs that are excluded from the initial cascade reconstruction. Even though the event is not fully contained, its visible energy can still be inferred on the basis of the signature that was detected.

The visible energy is a critical parameter that is highly dependent on the amount of absorption and scattering in the ice surrounding the interaction vertex. Cascades are simulated under different hypotheses (vertex position and time, direction and energy), and predicted charge distributions of the DOMs are compared against observed distributions to find those that best match the data. Systematic uncertainties in bulk scattering and absorption parameters as well as ice anisotropy were taken into account^{16,41}. For the bulk scattering and absorption parameters, the event was reconstructed by scaling the absorption and scattering parameters up and down by 5%. This gave five distinct energies, each corresponding to a different bulk-ice variant. A linear regression of these five points gave a model for the reconstructed visible energy as a function of the scattering and absorption parameters.

Once this was established, an uncorrelated 5% uncertainty in scattering and absorption was propagated onto the reconstructed visible energy. This procedure was repeated for three variations of the ice anisotropy⁴¹, which gave three distinct energy posteriors. These were combined uniformly, assuming equal probabilities for each anisotropy model, to obtain the overall uncertainty on the visible energy due to ice modelling. A DOM-to-DOM variation of 10% is additionally incorporated through a regularization term in the likelihood. Finally, a uniform 10% global energy scale uncertainty is convolved with the previously obtained visible energy posterior probability density function (PDF).

In addition, the approximate Bayesian calculation (ABC) method⁹ returns a sample of event vertices and directions for each ice model.

Article

They are combined across the bulk-ice variants by keeping only samples that have a corresponding test statistic below a pre-computed threshold. Lower values of the test statistic indicate better agreement between data and the resimulated sample. The sample of directions is fitted to a Kent distribution⁴², while the sample of vertices is passed as a three-dimensional Gaussian prior for the second reconstruction step using early pulses.

The likelihood of observing early pulses at times t_i^j at a given DOM j is given by⁴³:

$$\mathcal{L}(\hat{\mathbf{r}}, \mathbf{x}_0, t_0) = \prod_j^{N_{\text{DOMs}}} \prod_i^{N_{\text{hits}}^j} \left\{ \frac{\alpha_j}{T_j} + (1 - \alpha_j) p(t_i^j | \hat{\mathbf{r}}, \mathbf{x}_0, t_0) \right\}, \quad (2)$$

where N_{DOMs} is the number of operational DOMs, N_{hits}^j is the number of early pulses at DOM j , α_j is the expected relative contribution of noise to the hits in DOM j , T_j is the time window considered for early pulses and $p(t_i^j | \hat{\mathbf{r}}, \mathbf{x}_0, t_0)$ is the photon arrival time PDF at DOM j for a given track hypothesis with direction $\hat{\mathbf{r}}$ and position \mathbf{x}_0 at time t_0 . The photon arrival time PDFs are obtained by interpolating the results from dedicated MC simulations using spline functions^{10,44}. The posterior distribution of the track parameters is given by:

$$p(\hat{\mathbf{r}}, \mathbf{x}_0, t_0 | t_i^j) = \frac{\mathcal{L}p(\hat{\mathbf{r}}, \mathbf{x}_0, t_0)}{\int \mathcal{L}p(\hat{\mathbf{r}}, \mathbf{x}_0, t_0) d\hat{\mathbf{r}} d\mathbf{x}_0 dt_0}, \quad (3)$$

where the prior $p(\hat{\mathbf{r}}, \mathbf{x}_0, t_0) = p(\hat{\mathbf{r}})p(\mathbf{x}_0)p(t_0)$ assumes independence between groups of parameters. The prior on the position $p(\mathbf{x}_0)$ is taken from vertex posterior of the cascade reconstruction, the prior on the direction $p(\hat{\mathbf{r}})$ is a uniform distribution on the sphere, and the prior on the time $p(t_0)$ is a broad Gaussian centred on the vertex time of the cascade reconstruction. Samples from the posterior distribution are obtained using nested sampling with the dynesty package⁴⁵, assuming a flat prior for the direction and using the ABC output as a prior for the starting position. The three blue contours shown in Extended Data Fig. 2 correspond to the three anisotropy-model variants, which give different vertex priors. The muonic component of a hadronic cascade consists of a distribution of muons with different trajectories. The posterior distribution of the track direction is thus to be understood as the average direction of the muonic component. Using MC simulations of hadronic cascades, the coverage of the directional posterior was verified with respect to the direction of the initial shower.

From Extended Data Fig. 2, it is apparent that the cascade reconstruction is more sensitive to ice modelling than the hybrid reconstruction. Their best fits have a separation of about five degrees. The likelihood of the hybrid reconstruction is bimodal, with one mode in each lobe.

In order to estimate the energy of the leading muon, we performed MC simulations of 6-PeV cascades with a muon of varying energy, E_μ . The direction and position of the cascade and the muon are sampled from the posterior distribution of the early pulse track reconstruction. For every simulated event, the number of strings N_s on which at least one DOM detected early pulses is recorded. This gives the probability of observing N_s strings with early-pulse DOMs for a given E_μ , $\mathcal{L}(N_s | E_\mu)$, shown in Extended Data Fig. 3. As E_μ increases, the muon can penetrate deeper into the detector thus increasing the probability of larger N_s .

Assuming a uniform prior over E_μ , we can construct $P(E_\mu | N_s = 1)$, where $N_s = 1$ is what was observed in data, and obtain the 68% highest posterior density over E_μ . Compared to a pure cascade simulation, the agreement of simulated first photon arrival times with data is also improved by including such muons, as shown in Extended Data Fig. 4.

Atmospheric background rejection

Combining the two reconstructions above allows for a better rejection of the atmospheric background hypothesis than achieved by relying solely on the BDT selection. For an atmospheric muon to reproduce the

event signature seen in the data, it must reach the depth of the detector and suffer a large stochastic loss over a short distance to emulate the initial cascade and have enough energy remaining to deposit early pulses. We took a numerical approach to calculate a conservative estimate of the number of such events expected over the data-taking period by accepting all such muons that intersect a cylinder of radius 800 m and height 1,600 m centred on IceCube. The total muon flux at the surface of the Earth was calculated using MCEq⁴⁶ with the SIBYLL2.3c hadronic interaction model⁴⁷ and the Gaisser-Hillas 3a primary spectrum⁴⁸. This flux was then propagated to the cylinder using tabulated probabilities—obtained from MC simulations assuming the parameterization for photonuclear interactions from ref. ⁴⁹ and the parameterization for the bremsstrahlung cross-section from ref. ⁵⁰—of a muon of a given energy at the Earth's surface reaching a particular depth in the ice^{51,52}. The expectation rate is the surface integral over the vector field of incoming muons. In differential form,

$$dN_\mu = \mathcal{L}(N_s = 1 | E_\mu^f) \mathcal{P}(E_\mu^f | E_\mu^c, 20\text{m}) \mathcal{L}(X | E_\mu^c) \mathcal{P}(E_\mu^c | E_\mu^i, D(\hat{\mathbf{r}}, z)) \times \Phi(E_\mu^i, \hat{\mathbf{r}}) \hat{\mathbf{r}} \cdot d\mathbf{S} d\Omega dE_\mu^i dE_\mu^c dE_\mu^f \quad (4)$$

where $\Phi(E_\mu^i, \hat{\mathbf{r}})$ is the flux of muons with energy E_μ^i and direction $\hat{\mathbf{r}}$ at ground level, $\mathcal{P}(E_\mu^c | E_\mu^i, D(\hat{\mathbf{r}}, z))$ is the PDF for a muon to have energy E_μ^c after travelling distance $D(\hat{\mathbf{r}}, z)$ in ice to reach depth z given initial energy E_μ^i , $\mathcal{P}(E_\mu^f | E_\mu^c, 20\text{m})$ the PDF for a muon to have energy E_μ^f after travelling 20 m (shower length) given initial energy E_μ^c , and \mathbf{S} denotes the area element of the cylinder. The likelihood $\mathcal{L}(X | E_\mu^c)$ is obtained by taking the visible energy posterior and dividing out the most-conservative, uniform prior.

Since the event is downgoing, the expected atmospheric neutrino background is much smaller than the sample average. This is because atmospheric neutrinos at PeV energies are typically accompanied by high-energy muons from the same air shower. These muons should deposit much more energy in the detector than allowed by early pulses. In order to compute the passing fraction, we used equation (3.15) in ref. ¹⁸ with $\mathcal{P}_{\text{light}}(E_\mu^f) = 1 - \mathcal{L}(N_s = 1 | E_\mu^f)$. This is then used to down-weight the atmospheric neutrinos in MC that pass the BDT selection.

Calculation of P value for Glashow resonance

A likelihood-ratio test under the null hypothesis of exclusively CC or NC astrophysical neutrino interactions was performed. As contributions from atmospheric background are negligible, this likelihood-ratio test quantifies the probability that the event did not originate from the Glashow resonance. The likelihood assumes the reconstructed energy is sampled from an inhomogeneous Poisson point process and is given by

$$\mathcal{L}(S) = e^{-(B+S)} \prod_{i=1} \{B \mathcal{P}_B(E_i) + S \mathcal{P}_S(E_i)\} \quad (5)$$

where $\mathcal{P}_S(E_i)$ ($\mathcal{P}_B(E_i)$) is the probability of detecting event i with reconstructed energy E_i under the signal (background) hypothesis, estimated by constructing an unbinned PDF incorporating the uncertainties shown in Fig. 3. The background normalization, B , is the sum of CC and NC expectations in 4.6 years of data taking. Assuming $\gamma_{\text{astro}} = 2.49$, the estimated neutrino deep inelastic scattering background with reconstructed energy between 4 PeV and 8 PeV is about 0.3. The signal normalization, S , is a free parameter with the null hypothesis being $S = 0$. The likelihood-ratio test statistic is then

$$\Gamma = \log \frac{\mathcal{L}(S = S_{\text{max}})}{\mathcal{L}(S = 0)} \quad (6)$$

Since the number of observed events is one, an analytical solution for maximizing the signal probability is

$$\frac{\partial \mathcal{L}}{\partial S} = 0 \Rightarrow S_{\text{max}} = 1 - B \frac{\mathcal{P}_B}{\mathcal{P}_S} \quad (7)$$

Pseudo-experiments under the null hypothesis are then generated by randomly sampling a set of pseudo-events from a Poisson distribution, assuming the background normalization, and then sampling the reconstructed energy for each pseudo-event from the background PDF. Extended Data Fig. 5 shows the distribution of Γ obtained from pseudo-experiments under the null hypothesis. A P value of 0.01 was obtained, assuming the spectral index $\gamma_{\text{astro}} = 2.49$ and $\Phi_{\text{astro}} = 7.0$ given in Extended Data Table 1, which corresponds to a rejection of the null hypothesis at (one-sided) 2.3σ .

For the softer spectrum with $\gamma_{\text{astro}} = 2.89$, the significance increases to 2.7σ . For the harder spectrum with $\gamma_{\text{astro}} = 2.28$, the significance becomes 1.6σ . The spectral dependence arises entirely from the deep inelastic scattering background, as the shape of the Glashow resonance is not affected by spectrum assumptions. However, a recent measurement of the electron and tau neutrino flux²⁴ has its best-fit spectral index at 2.53, softer than the global-fit result at 2.49.

The P -value calculation here does not incorporate the early pulse information. To do so requires a fully resimulated and processed sample that includes simulated photons produced by muon secondaries in the shower. However, neglecting this information should give a conservative P -value estimation as the reconstructed leading muon energy and muon multiplicity are both more consistent with a GR hypothesis than the CC alternative. Specifically, assuming the QGSJET-01C hadronic model⁵³, the reconstructed muon energy of $26.4^{+28.6}_{-12.4}$ GeV is more consistent with the quartiles (21, 38, 72) GeV from a 6-PeV hadronic shower than those from a 6.3-PeV CC electron neutrino interaction, (0.04, 1.2, 10) GeV.

Segmented flux fit

The segmented flux fit relies on the MC, which maps true-primary energy to reconstructed energy. The flux in each of the three true-energy bins is assumed to follow a E^{-2} power law with a floating normalization. Then, as a function of this flux, the expected event rates in four reconstructed-energy bins in the range 4 PeV to 8 PeV were computed assuming equation (1) for the GR cross-section and the calculation in ref.³² for the CC and NC cross-sections. The bin width is chosen to be larger than the energy reconstruction uncertainty. The fit is performed over these four reconstructed-energy bins; their expected event rates are dependent on the flux in the three true-energy bins. Comparing the expected event rates to the observation of a single event with reconstructed visible energy 6.05 ± 0.72 PeV, we obtain the measured flux normalization and 68% upper limits shown in Fig. 4. For each true-energy bin, uncertainties were obtained using the Feldman–Cousins construction⁵⁴ while treating the normalizations in the other two bins as nuisance parameters that are profiled over.

Data availability

The full event data, including the location of each DOM, the time and charge of all pulses associated with this event, and relevant calibration details are available at <https://doi.org/10.21234/gr2021>. Additionally, the 90% contour of the hybrid cascade+track reconstruction shown in Fig. 2 and the measured flux shown in Fig. 4 can be found at the same URL.

Code availability

Much of the analysis code is IceCube proprietary and exists as part of the IceCube simulation and production framework. IceCube open-source code can be found at <https://github.com/icecube>. Additional information is available from analysis@icecube.wisc.edu upon request.

39. IceCube Collaboration. Evidence for high-energy extraterrestrial neutrinos at the IceCube detector. *Science* **342**, 1242856 (2013).
40. Haack, C., Lu, L. & Yuan, T. Improving the directional reconstruction of PeV hadronic cascades in IceCube. *EPL Web Conf.* **207**, 05003 (2019).
41. Chirkin, D. & Rongen, M. Light diffusion in birefringent polycrystals and the IceCube ice anisotropy. In *Proc. 36th Int. Cosmic Ray Conf. (ICRC2019)* 854 (Proceedings of Science, 2019).
42. Kent, J. T. The Fisher-Bingham distribution on the sphere. *J. R. Stat. Soc. B* **44**, 71–80 (1982).
43. Ahrens, J. et al. Muon track reconstruction and data selection techniques in AMANDA. *Nucl. Instrum. Methods A* **524**, 169–194 (2004).
44. Whitehorn, N., van Santen, J. & Lafebre, S. Penalized splines for smooth representation of high-dimensional Monte Carlo datasets. *Comput. Phys. Commun.* **184**, 2214–2220 (2013).
45. Speagle, J. S. dynesty: a dynamic nested sampling package for estimating Bayesian posteriors and evidences. *Mon. Not. R. Astron. Soc.* **493**, 3132–3158 (2020).
46. Fedynitch, A. et al. A state-of-the-art calculation of atmospheric lepton fluxes. In *Proc. 35th Int. Cosmic Ray Conf. (ICRC2017)* 1019 (Proceedings of Science, 2018).
47. Riehn, F. et al. The hadronic interaction model SIBYLL 2.3c and Feynman scaling. In *Proc. 35th Int. Cosmic Ray Conf. (ICRC2017)* 301 (Proceedings of Science, 2018).
48. Gaisser, T. K., Stanev, T. & Tilav, S. Cosmic ray energy spectrum from measurements of air showers. *Front. Phys.* **8**, 748–758 (2013).
49. Abramowicz, H. & Levy, A. The ALLM parameterization of $\sigma_{\text{tot}}(v^*p)$: an update. Preprint at <https://arxiv.org/abs/hep-ph/9712415> (1997).
50. Kelner, S. K., Kokoulin, R. P. & Petrukhin, A. A. About cross-section for high energy muon bremsstrahlung. Preprint at <https://lss.fnal.gov/archive/other/fprint-95-36.pdf> (1995).
51. Chirkin, D. & Rhode, W. Propagating leptons through matter with Muon Monte Carlo (MMC). Preprint at <https://arxiv.org/abs/hep-ph/0407075> (2004).
52. Koehne, J. et al. PROPOSAL: a tool for propagation of charged leptons. *Comput. Phys. Commun.* **184**, 2070–2090 (2013).
53. Kalmykov, N. N., Ostapchenko, S. S. & Pavlov, A. I. Quark-gluon string model and EAS simulation problems at ultra-high energies. *Nucl. Phys. B* **52**, 17–28 (1997).
54. Feldman, G. J. & Cousins, R. D. A unified approach to the classical statistical analysis of small signals. *Phys. Rev. D* **57**, 3873–3889 (1998).
55. Schneider, A. Characterization of the astrophysical diffuse neutrino flux with IceCube high-energy starting events. In *Proc. 36th Int Cosmic Ray Conf. (ICRC2019)* 1004 (Proceedings of Science, 2019).

Acknowledgements We thank T. Pierog, D. Heck and C. Baus for discussions on realistic hadronic shower simulations in ice. We gratefully acknowledge support from the following agencies and institutions: USA—the US National Science Foundation–Office of Polar Programs, the US National Science Foundation Physics Division, the Wisconsin Alumni Research Foundation, the Center for High Throughput Computing (CHTC) at the University of Wisconsin–Madison, the Open Science Grid (OSG), the Extreme Science and Engineering Discovery Environment (XSEDE), the Frontera computing project at the Texas Advanced Computing Center, the US Department of Energy–National Energy Research Scientific Computing Center, the Particle Astrophysics Research Computing Center at the University of Maryland, the Institute for Cyber-Enabled Research at Michigan State University, and the Astroparticle Physics Computational Facility at Marquette University; Belgium—the Funds for Scientific Research (FRS-FNRS and FWO), the FWO Odysseus and Big Science programmes, and the Belgian Federal Science Policy Office (Belspo); Germany—the Bundesministerium für Bildung und Forschung (BMBF), the Deutsche Forschungsgemeinschaft (DFG), the Helmholtz Alliance for Astroparticle Physics (HAP), the Initiative and Networking Fund of the Helmholtz Association, the Deutsches Elektronen Synchrotron (DESY), and the High Performance Computing Cluster of RWTH Aachen; Sweden—the Swedish Research Council, the Swedish Polar Research Secretariat, the Swedish National Infrastructure for Computing (SNIC), and the Knut and Alice Wallenberg Foundation; Australia—the Australian Research Council; Canada—the Natural Sciences and Engineering Research Council of Canada, Calcul Québec, Compute Ontario, the Canada Foundation for Innovation, WestGrid, and Compute Canada; Denmark—the Villum Fonden, the Danish National Research Foundation (DNRF), the Carlsberg Foundation; New Zealand—the Marsden Fund; Japan—the Japan Society for Promotion of Science (JSPS) and the Institute for Global Prominent Research (IGPR) of Chiba University; Korea—the National Research Foundation of Korea (NRF); Switzerland—the Swiss National Science Foundation (SNSF); the UK—the Department of Physics, University of Oxford.

Author contributions The IceCube neutrino observatory was constructed and is maintained by the IceCube Collaboration. A large number of authors contributed to the data processing, detector calibration and MC simulations used in this work. The IceCube collaboration acknowledges the substantial contributions to this manuscript from L.L., T.Y. and C. Haack. The final manuscript was reviewed and approved by all authors.

Competing interests The authors declare no competing interests.

Additional information

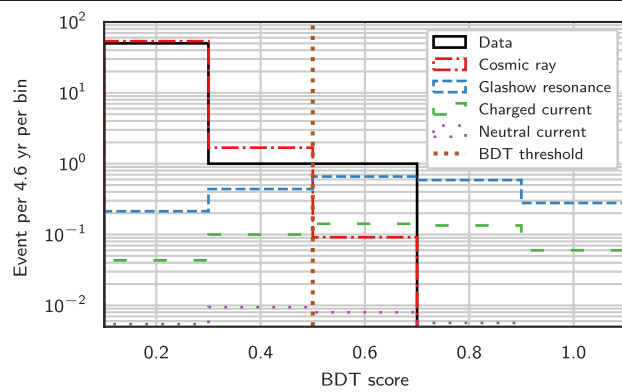
Correspondence and requests for materials should be addressed to The IceCube Collaboration.

Peer review information Nature thanks Sergio Navas and the other, anonymous, reviewer(s) for their contribution to the peer review of this work.

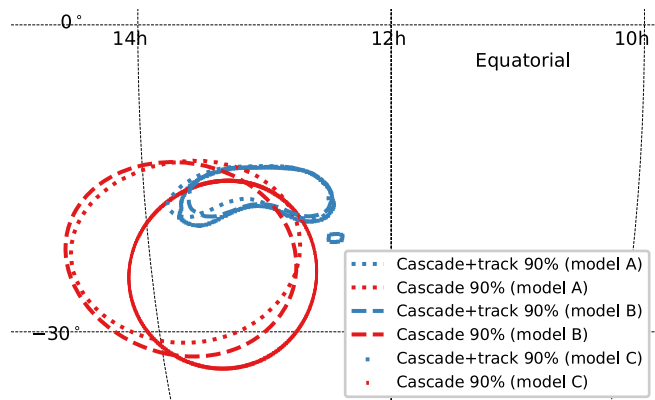
Reprints and permissions information is available at <http://www.nature.com/reprints>.

37. Cowen, D. Tau neutrinos in IceCube. *J. Phys. Conf. Ser.* **60**, 227–230 (2007).

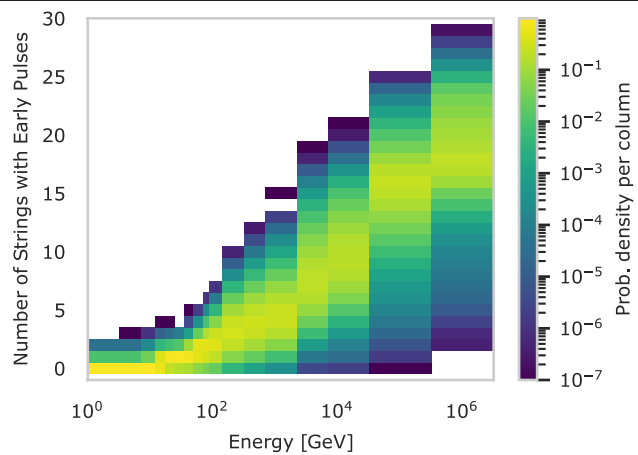
38. Aartsen, M. G. et al. First observation of PeV-energy neutrinos with IceCube. *Phys. Rev. Lett.* **111**, 021103 (2013).



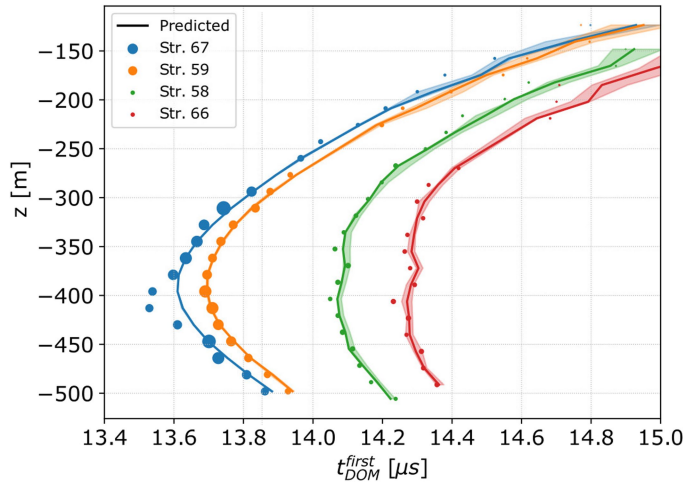
Extended Data Fig. 1 | The BDT distribution for events with a reconstructed energy above 4 PeV. The plotted events are required to be consistent with a cascade hypothesis based on the goodness of fit. The PEPE event selection requires a BDT score greater than 0.5. Good data–MC agreements were observed across the background and the signal region. See Methods for details.



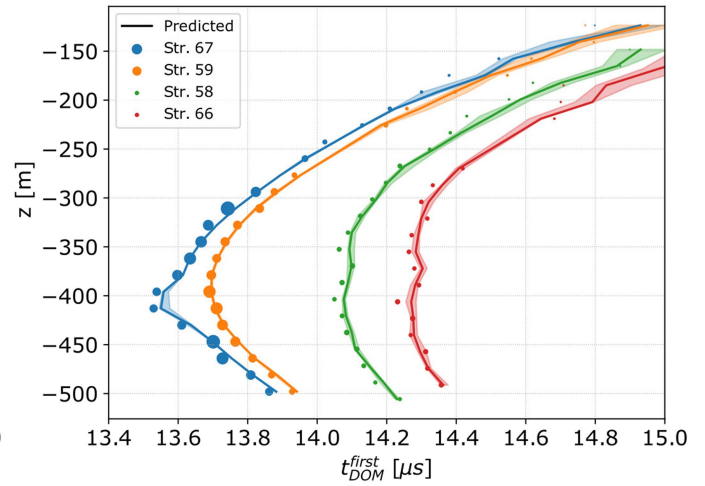
Extended Data Fig. 2 | Effect of ice anisotropy on the reconstructed direction. Shown are reconstructed directions assuming three different ice anisotropy models⁴¹ (A, B and C). While the cascade-based reconstructions (red) exhibit some shifts, the hybrid cascade+track reconstructions (blue) appear less susceptible to ice model differences.



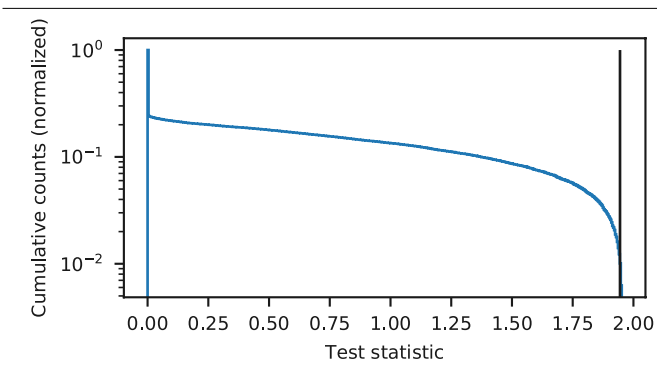
Extended Data Fig. 3 | The number of strings that observed early pulses for a given muon energy. The colour scale shows the probability of observing the number of strings with early pulses, N_s , as function of the simulated muon energy.



Extended Data Fig. 4 | First-photon arrival times on four strings. Left, first-photon arrival times (t_{DOM}^{first}) on photosensors deployed on four strings ('Str.', shown in different colours) nearest to the reconstructed vertex plotted against their depth relative to the centre of IceCube (z). Observed times are shown as circles, with the size of each circle corresponding to the total charge on that DOM. Predicted arrival times assuming a cascade without escaping



muons are shown as lines with shaded regions corresponding to the quartiles obtained from repeated resimulations. Three DOMs on string 67 stand out and have first-photon arrival times that are inconsistent with predictions. Right, with the addition of a highly relativistic muon, much better consistency is obtained between observed and predicted first-photon arrival times on the three DOMs with early pulses.



Extended Data Fig. 5 | The test statistic distribution under the null hypothesis. Cumulative distribution of f under the null hypothesis, as generated under the sampling scheme described in the text. The test statistic for the data event is shown in black.

Extended Data Table 1 | Expected event rates for hadronic decay of the W^- in IceCube

γ_{astro}	2.28	2.49	2.89
Φ_{astro}	4.32	7.0	6.45
PEPE pp	2.27	1.55	0.28
HESE pp	1.15	0.79	0.14
PEPE $p\gamma$	1.01	0.69	0.12
HESE $p\gamma$	0.51	0.35	0.06

Expected event rates for the hadronic channel from the Glashow resonance decay using 4.6 years of data. The values of spectral index γ_{astro} and flux normalization Φ_{astro} are from refs. ^{2,21,55} (a recent update²² has slightly shifted the best-fit values of γ_{astro} and Φ_{astro} given in ref. ⁵⁵; it is pending publication). The units of Φ_{astro} are $10^{-18} \text{ GeV}^{-1} \text{ cm}^{-2} \text{ s}^{-1} \text{ sr}^{-1}$.